OPEN ACCESS

International Journal of Physical Sciences

16 April 2018
ISSN 1992-1950
DOI: 10.5897/IJPS
www.academicjournals.org

ACADEMIC JOURNALS
expand your knowledge

ABOUT IJPS

The **International Journal of Physical Sciences (IJPS)** is published weekly (one volume per year) by Academic Journals.

International Journal of Physical Sciences (IJPS) is an open access journal that publishes high-quality solicited and unsolicited articles, in English, in all Physics and chemistry including artificial intelligence, neural processing, nuclear and particle physics, geophysics, physics in medicine and biology, plasma physics, semiconductor science and technology, wireless and optical communications, materials science, energy and fuels, environmental science and technology, combinatorial chemistry, natural products, molecular therapeutics, geochemistry, cement and concrete research, metallurgy, crystallography and computer-aided materials design. All articles published in IJPS are peer-reviewed.

Contact Us

Editorial Office: ijps@academicjournals.org

Help Desk: helpdesk@academicjournals.org

Website: http://www.academicjournals.org/journal/IJPS

Submit manuscript online http://ms.academicjournals.me/

Editors

Editorial Board

International Journal of Physical Sciences

Table of Contents: Volume 13 Number 7, 16 April, 2018

ARTICLES

academicJournals

Vol. 13(7), pp. 106-111, 16 April, 2018
DOI: 10.5897/IJPS2017.4670
Article Number: A97C90A56658
ISSN 1992 - 1950

http://www.academicjournals.org/IJPS

International Journal of Physical Sciences

Full Length Research Paper

Investigating influence of the phases of solar activity cycle 23 on coronal mass ejections transit time

Ojih Victoria B.[1*] and Okeke Francisca N.[2]

[1]Department of Physics, Federal College of Education (Technical), Asaba, Delta State, Nigeria.
[2]Department of Physics and Astronomy, University of Nigeria, Nsukka, Enugu State, Nigeria.

Received 14 August, 2017; Accepted 9 March, 2018

It has been established that Coronal Mass Ejections (CMEs) follow the phase of solar activity cycle. CMEs are known to be the major cause of geomagnetic storms which have devastating effects on earth atmosphere. Predicting their arrival times has been a major issue in space weather forecast. Influence of the phases solar activity cycle 23 on CMEs transit time were investigated using fast CMEs data with initial speed ≥ 900 kms^{-1} that were associated with intense geomagnetic storm obtained from Large Angle Spectrometric Coronagraph (LASCO) aboard the Solar and Heliospheric Observatory (SOHO) for solar cycle 23. Empirical Coronal Mass Ejections Arrival (ECA) model equations of Ojih-Okeke modified model, Gopalswamy 2000 model (G2000), Gopalswamy 2001 model (G2001), and Vrsnak and Gopalswamy 2002 model (VG2002) were applied to the data points. Scatter plots of CMEs transit time as function of CMEs initial speed and solar wind speed were generated. Linear correlation coefficients were obtained. The significance of the correlation was tested at 0.05 level of significant. Linear correlation coefficients obtained for solar maximum period of solar cycle 23 for Ojih-Okeke model, VG2002 model, G2001 model and G2000 model were -0.63, -0.82, -0.78 and -0.79 respectively and those obtained for declining phase of solar cycle 23 were -0.93, -0.80, -0.80 and -0.86 respectively. There is no significant difference between the correlations obtained for solar maximum phase and the declining phase of solar cycle 23. The findings depict that phases of solar activity cycle has no significant influence on CMEs transit time.

Key words: Coronal mass ejections, solar activity cycle, transit time, phase, geomagnetic storm.

INTRODUCTION

Coronal mass ejections (CMEs) are huge explosions of solar materials (clouds of plasma and magnetic fields) from the sun that are released into space. Over a distance of a few solar radii, CMEs may accelerate up to a speed of 300 0 Kms^{-1} and subsequently propagate through the solar wind away from the Sun (Mostl et al., 2014; Yashiro et al., 2001). CMEs are known to be the major cause of severe geomagnetic disturbances which is often referred to as space weather (Zhang et al., 2001; Cheng et al., 2014; Cyr et al., 2000; Tripathi and Mishra,

*Corresponding author. E-mail: ojihvictoria@gmail.com. Tel: 08038739080.

2005). There are several space weather phenomena which tend to be associated with or are caused by geomagnetic storm. These include: Solar Energetic Particles (SEP) events (hazardous to Humans), Geomagnetically Induced Currents (GIC) which cause damages to satellites and electricity grid, ionospheric disturbances which may lead to radio and radar scintillation, disruption of navigation by magnetic compass and aurora displays at much lower latitudes than normal (Baker and John, 2008).

The activity of the sun is measured by the number of sunspots appearing on its surface. The number of the sunspot increases and decreases over time in approximately 11 years called the solar cycle. Scientists are more interested in the solar cycle maximum and its minimum because they mark the peak and the least of the solar activity. Tripathi and Mishra (2005) observed that the occurrence frequency of CMEs generally follow the phase of solar cycle. Carol and Dale (2007) also established that the occurrence rate of CMEs increases with increasing solar activity, its peak occurs during solar maximum, and CMEs can occur at any time during the solar cycle. Kim et al. (2007) also asserted that CMEs tend to tag along with solar activity cycle having its highest occurrence in solar maximum and its lowest during solar minimum.

Several models have been developed to predict the arrival time of CMEs from sun to the earth. There are still deviations observed between the results from the models compared to the observed transit time of the CMEs. Since occurrence of CMEs has been observed to follow the phase of solar cycle, could it be that the phases of solar activity cycle have any influence on CMEs arrival time? Predicting the arrival time of CMEs with minimal average error has been a major issue in space weather forecast. Predicting the arrival time of CMEs with minimal average error will help serve as a practical way of getting advance warning of solar disturbances heading towards the earth, saving billions of Naira and Dollars in USA etc that would have been used to repair or replace damaged satellites and power grids, identify communication problems, help high altitude flight management and make provisions for renewable energy sources to protect the Earth against a black out. The aim of this study therefore is to investigate the influence of solar activity cycle on CMEs transit time.

METHODOLOGY

Sources of data

The coronal mass ejections data were obtained from coronagraph observations of Large Angle Spectroscopic on Solar and Heliospheric Observatory (SOHO/LASCO) CME catalog on website https://cdaw.gsfc.nasa.gov/CME-list/ for solar activity cycle 23 (1999-2002). The geomagnetic storm data were obtained from the World Data Centre (WDC) for geomagnetism, Kyoto Japan on website wdc.kugi.kyoto-u.ac.jp> dstdir. We selected CMEs with initial speed U ≥ 900 kms^{-1} associated with disturbance storm time index (Dst ≤ 100 nT). The disturbance storm time index is a measure of geomagnetic activities storm use to access the severity of magnetic storms. Dst ≤ -100 nT denotes intense geomagnetic storm.

Coronal mass ejections data

Table 1 presents Coronal Mass Ejection data with initial speed ≥ 900 kms^{-1} associated with intense geomagnetic storm observed for the period of solar activity cycle 23. Column 1 is the date of CME event, Column 2 is Onset time of the CME, column 3 represents the CMEs initial speed and column 4 is the Dst index.

Empirical coronal mass ejection model equations

Gopalswamy et al. (2000) Model: Constant acceleration or deceleration

The author assumed that the acceleration was constant between the sun and 1AU (AU is astronomical unit, 1AU is sun – earth distance) so that the total transit time of CMEs from sun to earth is given by;

$$\tau = \frac{-U+\sqrt{U^2+2\,a_2 S}}{a_2} \quad (1)$$

where τ is time taken by CME to travel from sun to earth, U is the CME initial speed, a_2 is acceleration, $a_2 = 10^{-3}(0.0054U-2.2)$ and S is the distance between the sun and the earth.

Gopalswamy et al. (2001) Model: Cessation of acceleration before IAU

The model assumes that interplanetary coronal mass ejection (ICME) acceleration ceased at a heliocentric distance of 0.76AU for all CMEs irrespective of their initial speed. Therefore the total transit time to IAU is the sum of the travel time to 0.76AU at constant acceleration, and the travel time from 0.76AU to IAU at constant speed. The total transit time from sun to 1AU is given by;

$$\tau = \frac{-U+\sqrt{U^2+2a_2 d}}{a_2} + \frac{IAU-d}{\sqrt{U^2+2a_2 d}} \quad (2)$$

where d is acceleration cessation distance, d = 0.076AU, U is CMEs initial speed and a_2 is acceleration.

Vrsnak and Gopalswammy (VG) Model (2002 Model): Aerodynamic drag force

The model was proposed for estimating the ICME transit time when the only force acting upon the ICME in interplanetary space is the aerodynamic drag

$$\tau = \frac{r_{sR}}{V} + \frac{10 r_s}{U} \quad (3)$$

where τ is the transit time from sun to earth, r is heliocentric radius, r_s is solar radius, R is heliocentric distance. ($R = \frac{r}{r_s}$), U is the CMEs initial speed and V is the CMEs speed at R=10.

Ojih-Okeke modified coronal mass ejection arrival model (Ojih and Okeke, 2017)

Authors assumed that the fast CMEs undergo (1) three phases as

Table 1. Coronal mass ejections data with Dst ≤ - 100 nT, U ≥ 900 km s^{-1}.

S/N	CME Event Date	CME Onset Time (UT)	CME initial speed U (kms^{-1})	Solar wind speed W(kms^{-1})	Dst (nT)
1	10/2/2000	2:30	944	590	-133
2	4/04/2000	16:33	1188	620	-280
3	14/07/2000	10:54	1674	1040	-301
4	16/09/2000	5:18	1215	840	-201
5	10/04/2001	5:30	2411	740	-271
6	19/10/2001	16:50	901	680	-187
7	28/10/2001	15:26	1092	510	-157
8	4/11/2001	16:35	1810	750	-292
9	22/11/2001	23:30	1437	1040	-221
10	17/04/2002	8:26	1240	640	-149
11	22/05/2002	3:26	1557	920	-109
12	16/08/2002	12:30	1585	580	-106
13	5/09/2002	16:54	1748	550	-181
14	29/09/2002	15:08	956	410	-174
15	28/05/2003	0:50	1366	760	-144
16	28/10/2003	8:50	2459	1900	-422
17	18/11/2003	0:06	1660	700	-130
18	20/01/2004	14:54	965	680	-170
19	25/7/2004	16:54	1333	1000	-263
20	7/11/2004	17:12	1759	810	-247
21	13/5/2005	1:30	1689	950	-216
22	22/8/2005	19:48	1194	710	-139
23	9/9/2005	2:54	2257	1100	-162
24	13/12/2006	4:12	1774	900	-107

they travel from sun to earth: a deceleration which ceases before 0.1 AU, a constant speed propagation until about 0.45AU and a gradual deceleration that continues beyond 1AU. (2) That 0.45AU, the CMEs have decelerated to solar wind speed. Total transit time of CMEs from sun to earth is given by:

$$\tau = \frac{-U+\sqrt{U^2+2\,a_1 d_1}}{a_1} + \frac{d_2}{\sqrt{U^2+2\,a_1 d_1}} + \frac{-W+\sqrt{W^2+2\,a_2 d_3}}{a_2} \quad (4)$$

Where d_1 is 0.08AU, d_2 is (0.45AU - 0.08AU), d_3 is 1AU - 0.45AU); $a_1 = 10^{-3}$(0.0054U - 2.2), $a_2 = 10^{-3}$(0.0054W - 2.2); a_1 is acceleration for first stage of CMEs' propagation, a_2 is acceleration for the third stage of the CMEs' propagation and W is solar wind speed.

The three empirical coronal mass ejection arrival model equations of Gopalswammy (Equations 1, 2 and 3) and the Ojih-Okeke modified coronal mass ejection arrival model (Equation 4) were applied to the CMEs data obtained for solar maximum period of solar cycle 23 and for the declining phase of solar cycle 23 to obtain the predicted CMEs transit time. Scatter plots of the CMEs predicted transit time as a function of CMEs initial speed were generated for each model. Linear correlation coefficient of each plot was determined. The significance of correlation was tested at 0.05 level of significant.

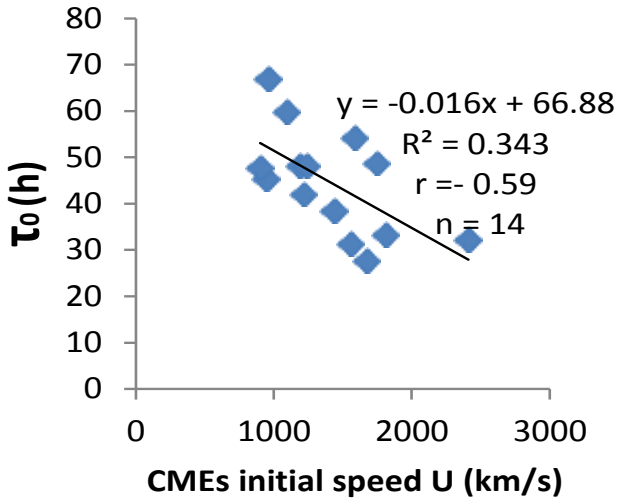

Figure 1. A plot of CMEs observed transit time as a function of CMEs initial speed for solar maximum period of solar activity cycle 23 (1999-2002).

RESULTS AND DISCUSSION

Figure 1 showed a scatter plot of CMEs observed transit time as function of CMEs initial speed for solar maximum period of solar activity cycle 23. The linear correlation coefficient obtained from the plot is -0.59 with p- value

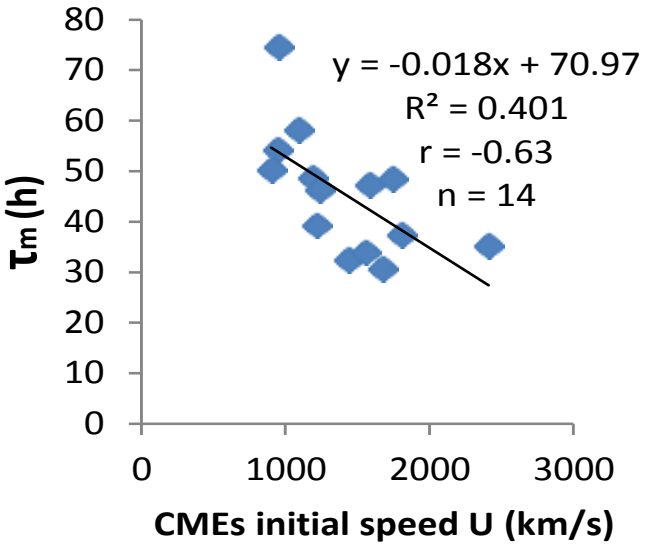

Figure 2. A plot of CMEs predicted transit time as a function of CMEs initial speed for Ojih-Okeke modified model for solar maximum period of solar activity cycle 23 (1999-2002)

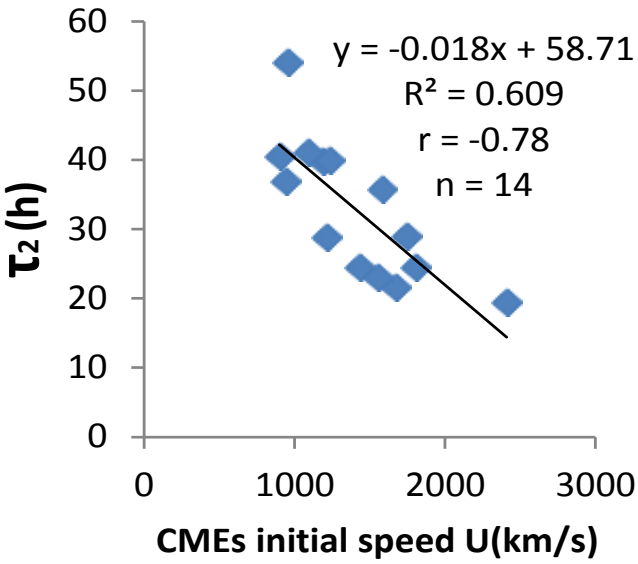

Figure 4. A plot of CMEs predicted transit time as a function of CMEs initial speed for G2001 model for solar maximum period of solar activity cycle 23 (1999-2002).

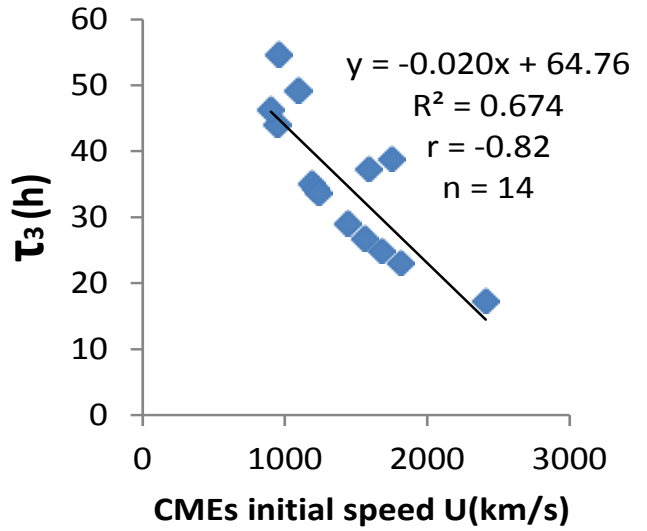

Figure 3. A plot of CMEs predicted transit time as a function of CMEs initial speed for VG2002 model for solar maximum period of solar activity cycle 23 (1999-2002).

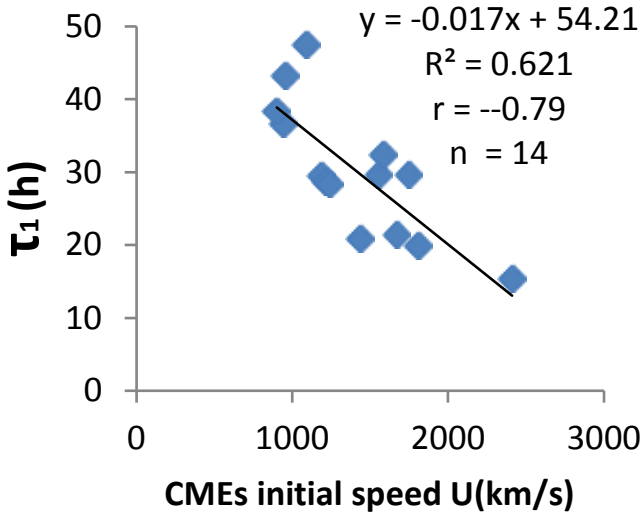

Figure 5. A plot of CMEs predicted transit time as a function of CMEs initial speed for G2000 model for solar maximum period of solar activity cycle 23 (1999-2002).

0.045. This p- value is less than 0.05 indicating that the correlation is significant. Figure 2 is a scatter plot of CMEs predicted transit time as a function of CMEs initial speed for Ojih-Okeke model for solar maximum period of solar activity cycle 23. The linear correlation coefficient obtained for the plot is -0.63 with p-value 0.003 which is less than 0.05. This shows that the correlation is significant. Figure 3 is a scatter plot of CMEs predicted transit time as a function of CMEs initial speed for VG2002 model for solar maximum period of solar cycle 23. The linear correlation coefficient obtained from the plot is -0.82 with p-value 0.001. This value is less than 0.05 which implies that the correlation is significant. Figure 4 is a scatter plot of CMEs predicted transit time as a function of CMEs initial speed for G2001 model. The linear correlation coefficient obtained from the plot is -0.78 with p-value 0.001 which is less than 0.05. This value depicts that correlation is significant. Figure 5 shows a scatter plot of CMEs predicted transit time as a function of CMEs initial speed for G2000 model. The

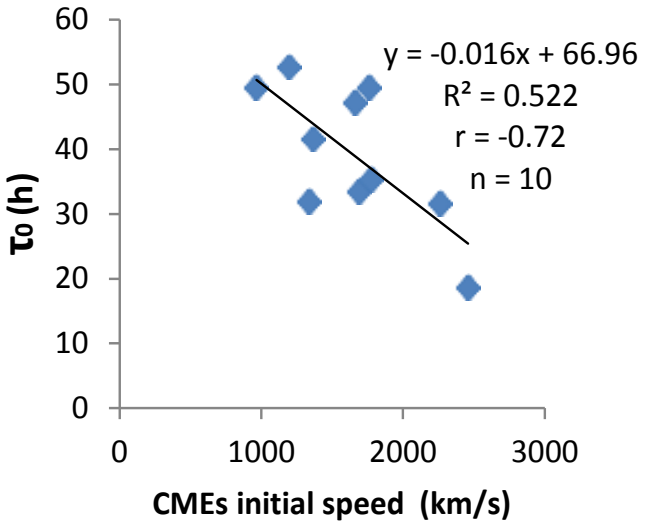

Figure 6. A plot of observed transit time as a function of CMEs initial speed for the declining phase of solar activity cycle 23 (2003-2006).

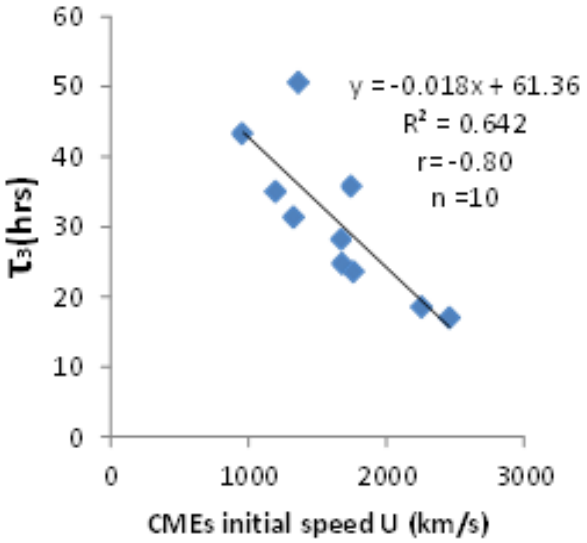

Figure 8. A plot of CMEs predicted transit time as a function of CMEs initial speed for VG2002 model for the declining phase of solar activity cycle 23 (2003-2006).

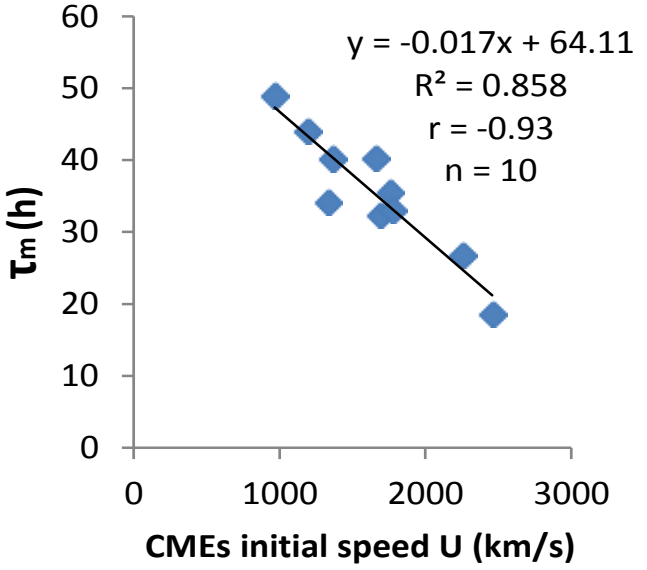

Figure 7. A plot of CMEs predicted transit time as a function of CMEs initial speed for Ojih-Okeke modified model for the declining phase of solar activity cycle 23 (2003-2006).

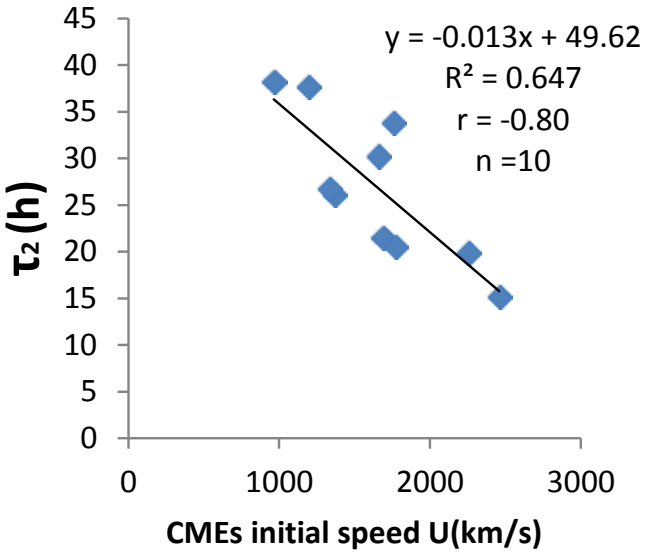

Figure 9. A plot of CMEs predicted transit time as a function of CMEs initial speed for G2001 model for the declining phase of solar activity cycle 23 (2003-2006).

linear correlation coefficient of the plot is -0.79. The p-value is 0.001. This value is less than 0.05 which also depicts that the correlation is significant.

Figure 6 is a scatter plot of CMEs observed transit time as a function of CMEs initial speed for the declining phase of solar activity cycle 23 (2003-2006). Linear correlation coefficient obtained for the plot is -0.72 with p-value of 0.021 which is less than 0.05. This shows that correlation is significant. Figures 7, 8, 9 and 10 are scatter plots of CMEs predicted transit time as functions of CMEs initial speed for Ojih-Okeke modified model, VG2002 model, G2001 model and G2000 model respectively. The linear correlation coefficient for Ojih-Okeke model is -0.93, -0.80 for VG2002 model, -0.80 for G2001 model and -0.86 for G2000 model. The p- values are 0.001, 0.001, 0.001 and 0.001 respectively. The p-values are all less than 0.05 indicating that correlations are significant.

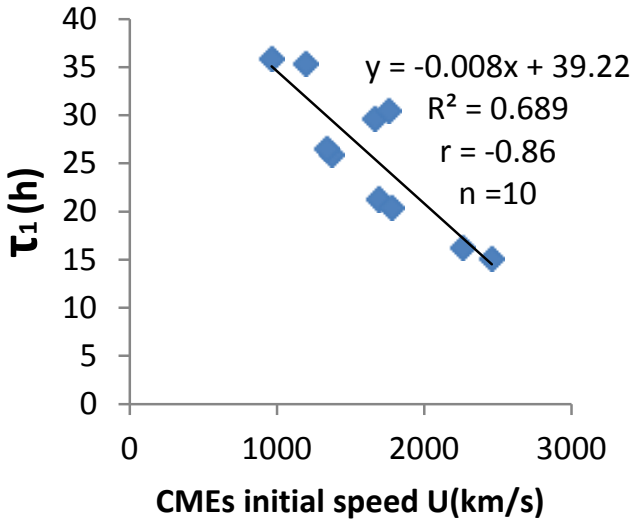

Figure 10. A plot of CMEs predicted transit time as a function of CMEs initial speed for G2000 model for the declining phase of solar activity cycle 23 (2003-2006).

CONCLUSION AND RECOMMENDATION

Influence of phases of solar activity cycle on coronal mass ejections transit time was investigated using solar cycle 23. CMEs data with initial speed ≥ 900 kms^{-1} associated with intense geomagnetic storm obtained from Large Angle Spectrometric Coronagraph (LASCO) aboard the Solar and Heliospheric Observatory (SOHO) during solar cycle 23 were used. Empirical Coronal Mass Ejections Arrival (ECA) model equations of Ojih-Okeke modified model, Vrsnak and Gopalswamy 2002 (VG2002) model, Gopalswamy 2001 (G2001) model and Gopalswamy 2000 (G2000) model were applied to the CMEs data. Scatter plots of CMEs transit time as function of CMEs initial speed were generated. Linear correlation coefficients obtained from the plots were tested at 0.05 level of significant. The findings reveal that there is no significant difference, between the correlation coefficients obtained for solar maximum phase of the solar cycle 23 and the declining phase of the solar activity cycle 23. Therefore the phases of solar activity cycle have no significant influence on CMEs transit time. It is recommended that ECA models be employed in predicting arrival times of CMEs most especially the Ojih-Okeke model which has been proven to have yielded a better result.

CONFLICT OF INTERESTS

The authors have not declared any conflict of interests.

ACKNOWLEDGEMENT

The authors are grateful for the use of geomagnetic storm data from the world data centre for Geomagnetism Kyoto Japan and the use of the CME catalog generated and maintained at the CDAW Data centre by NASA and the Catholic University of America in Cooperation with the Naval Research laboratory.

REFERENCES

Baker DN, John K (2008). Severe space weather events – understanding societal and economic impacts. A Workshop Report of National Academies Press P 77.

Carol BW, Dale AO (2007). An introduction to modern Astophysics. San Francisco, Addison Wesley P 390.

Cheng L, Shen YZ, Bin A, Ye MP, Wang S (2014). Full Halo coronal mass ejections arrival at the earth. http:// space.ustc.edu. Cn /dreams/.fhcmes/.

Cyr OC, Raymond JC, Thompson BJ, Gopalswamy NK, Kahler SK, Lara N, claravella A, Romol N, Oneal R (2000). SOHO and Radio observation of CME shock Wave. Geophys. Res. Letters J. 27(10):1439-1442.

Gopalswamy N, Alejandro L, Russel AH (2001). Predicting the I-AU arrival times of coronal mass ejections. Geophys. Res. J. 106(A12):29-217.

Gopalswamy N, Lara A, Lepping RP, Kaiser ML, Berdichevsky D, Cyr OC (2000). Interplanetary acceleration of coronal mass ejections. Geophys. Res. Lett. J. 27:145.

Kim KH, YJ Moon, Cho KS (2007). Prediction of the 1-AU arrival times of CME-associated interplanetary shocks: Evaluation of an empirical interplanetary shock propagation model. J. Geophys. Res. 112:A05104.

Mostl CK, Amla JR, Hall PC, Liewer EM, Jong RC, Colaninno AM, Galvin AB (2014). Connecting speeds , directions and arrival time of 22 Coronal Mass Ejection from the Sun to 1AU. Astrophys. J. V5/2/11.

Ojih VB, Okeke FN (2017). Application of Ojih –Okeke modified Empirical Coronal Mass Ejections Arrival (ECA) model in predicting the arrival time of CMEs. Int. J. Phys. Sci. 12(16).

Tripathi RM, Mishra AP (2005). Characteristics features of CMEs with respect to their source region. Proceeding of the 29th International Cosmic Ray Conference, Pune, India 1:149.

Vrsnak B, Gopalswamy N (2002). Influence of aerodynamic drag on the motion interplanetary ejecta. J. Geophys. Res. 107:10.1029/2001/JA 000120.

Yashiro SN, Gopalswamy GM, Cyr OC, Plunkett SP, Rich NB, Howard RA (2001). A catalog of white light coronal mass ejections observed by the SOHO Spacecraft. J. Geophys. Res. 109(A):7105.

Zhang J, Wang T, Zhang C, Liu Y, Nitta N, Slater GL, Wang J (2001). Flare-CME events association with a super active region recent insight into the Physics of the Sun and heliosphere: Highlights from SOHO and other space missions. Pal Brekke (Eds), Proceedings of IAU Symposium. P 203.

academicJournals

Vol. 13(7), pp. 112-119, 16 April, 2018
DOI: 10.5897/IJPS2018.4723
Article Number: 9A540B656661
ISSN 1992 - 1950

http://www.academicjournals.org/IJPS

International Journal of Physical Sciences

Full Length Research Paper

A compact and sensitive avalanche photodiode-based gamma detection and spectroscopy system

Masroor H. S. Bukhari* and A. Rauf

Department of Physics, Faculty of Science, Jazan University, Gizan 45142, Jazan, Saudi Arabia.

Received 27 February, 2018; Accepted 13 March, 2018

This research presents the design of a simple and compact yet sensitive gamma detection system which finds optimal utility in student research and demonstration purposes. The design is based on an Avalanche Photodiode (APD), a compact solid-state device. It was argued that, by the virtue of its concise size, simplicity and lower cost, an APD based gamma detection system is a better alternative in these applications as compared to the high-cost and complex Photomultiplier (PMT) based detector systems. This paper provides the basic working details of our design and preliminary test results.

Key words: Avalanche photodiode (APD), gamma spectroscopy, scintillator.

INTRODUCTION

Gamma detection constitutes an important area of nuclear and particle physics and finds its use in all standard undergraduate physics laboratories. Often, student research projects entail some kind of gamma ray detection and spectroscopy system, but such systems are quite expensive and sophisticated. The purpose of this study was to develop a low-cost physics laboratory gamma detection system which was simple and students can build it too under teacher's supervision.

As a result of the study, we came up with the design of a simple Avalanche Photodiode (APD)-based gamma detection and spectroscopy system. This research design is based on a commercial APD (Webb and McIntyre, 1970; Wolff, 1954; Tsang, 1985; Razeghi, 2010) device, which is used in "Geiger mode" (Aull, 2016) to obtain a realistic and optimal design for the best possible single-photon gamma detection and spectroscopy system. APD's are some of the most sensitive forms of photodiodes and in many ways better than other photodetector devices such as PIN diodes; thus we could not find a better low-cost alternative to the PMT (Photomultiplier Tube) for our application. PMT's, other than their being expensive detectors, require a sophisticated detection system and high-voltage supplies of around 1500 – 2500 V, which can be cumbersome and expensive for small-scale college laboratories.

The APD and its readout circuitry are mounted on a Thermo-Electric Cooler (TEC) plate to cool down the heat generated from the APD while used in operation.

An organic scintillator is used in conjunction with the APD to convert the incident gamma rays into scintillations which could be detected and amplified by

*Corresponding author. E-mail: mbukhari@jazanu.edu.sa.

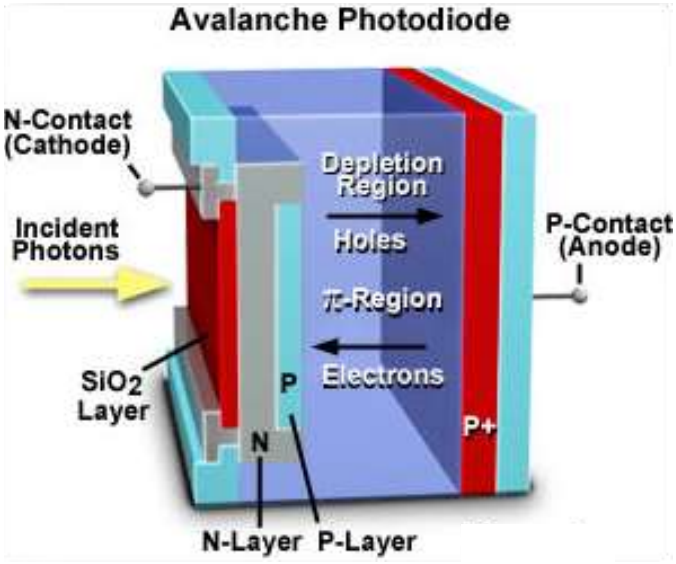

Figure 1. An overview and working of an Avalanche Photodiode structure.
Source: Courtesy and Copyright: Hamamatsu Corp.

Figure 2. Some kinds of APD's as used in particle and nuclear physics. The device at far left is the APD used in our study.
Source: Courtesy and Copyrights Photonix Corp.

the diode.

Final testing of the device is performed with a Cobalt-57 (^{57}Co) source to identify the system's detection capabilities.

APD MODE OF OPERATION

An APD works on the process of internal multiplication and avalanche generation (Webb and McIntyre, 1970; Wolff, 1954; Tsang, 1985). APDs are extremely sensitive and high-speed solid-state semiconductor photon detectors. Compared to other devices, such as PIN photodiodes, they have an intrinsic region (Figure 1) where the process of electron multiplication is carried out with a bias voltage. Detected photons create an electron-hole shower in the depletion layer of a silicon photodiode structure and the resulting electron-hole pairs move towards the respective PN junctions at a speed of up to 105 m per second, depending on the electric field strength.

A practical implementation of an APD diode is illustrated in Figure 1 (Courtesy Hamamatsu Corp.), whereas Figure 2 illustrates a view of some commercially-available APD devices (Courtesy Photonix Corp.). Gain for such commercially available devices is typically in the range from x10 to x300, but there are APDs available from specialist manufacturers with gains of thousands. This can then give a significant advantage over regular PIN photodiodes for applications

The APD Gain (M), also known as multiplication factor, can be expressed as (Tsang, 1985);

$$M = \frac{1}{1 - \int_0^L \alpha(x)\, dx} \tag{1}$$

where *L* is the space-charge boundary for electrons, and α (x) is the multiplication coefficient for electrons (and holes).

The excess noise (E) at a given M, during the avalanche process, is expressed as (Tsang, 1985);

$$\mathrm{ENF} = \kappa M + \left(2 - \frac{1}{M}\right)(1 - \kappa) \tag{2}$$

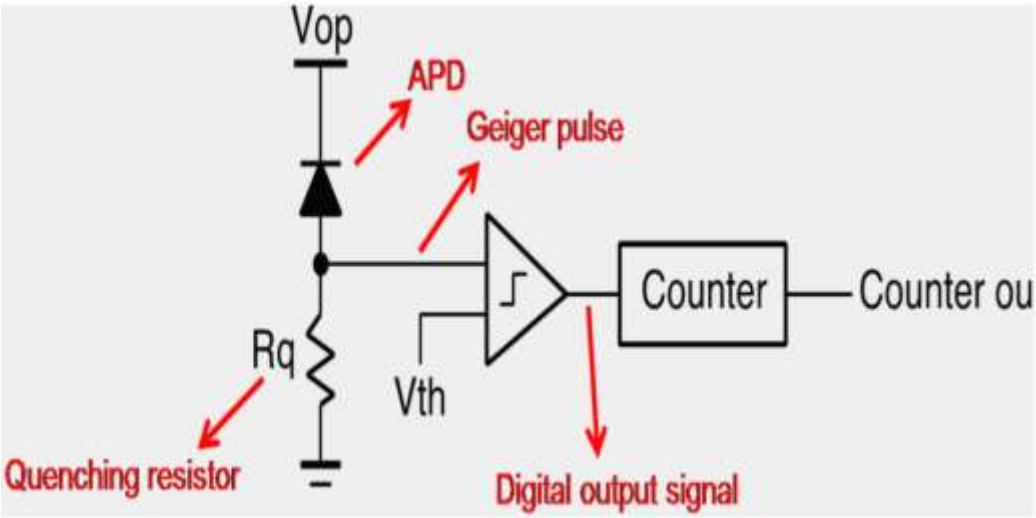

Figure 3a. An APD design in Geiger Mode with a quenching circuit (Image Courtesy with Thanks: Ecole Federal Polytechnique Lausanne).
Source: https://aqua.epfl.ch/page-96295-en.html.

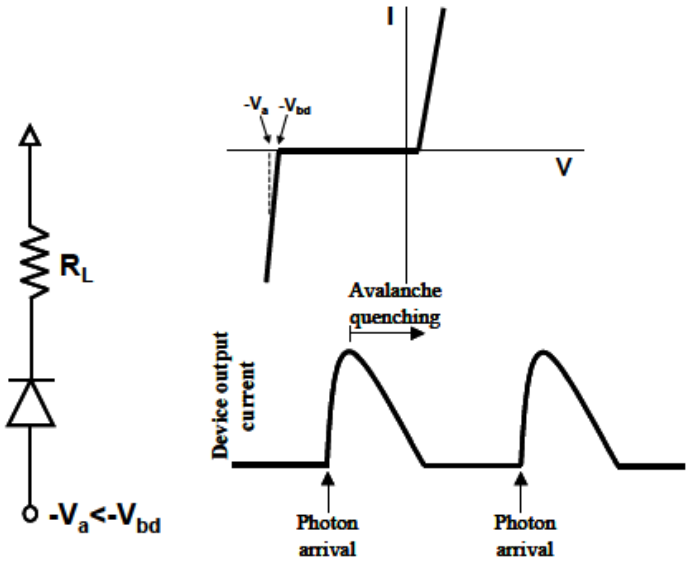

Figure 3b. Basic APD detection circuit in Geiger Mode.
Source: Reproduced with thanks from Razeghi (2010).

where κ is the ratio of the hole impact ionization rate to that of electrons.

THE SYSTEM DESIGN

This research design is based upon a commercially available simplest possible APD device which is operated in the "Geiger Mode" operation (Claycomb, 2016). When biased above the breakdown voltage, that is, in the Geiger Mode, the avalanche photodiodes are capable of detecting single photons. This operation mode is called Geiger mode for analogy with the x-ray detection and the APDs that show this capability are called single-photon avalanche diodes (SPADs).

In order to reach those capabilities, the APD must be connected to a quenching circuit (Figure 3), which should be able to attenuate the avalanche multiplication and subsequent current increase after the detected photons are registered.

The simplest passive quenching circuit is a resistor connected in series with the APD (Figure 3a and b). With the help of this technique an incident photon is absorbed in the window of the negatively biased APD, and by means of consecutive multiplication events, the initial charge is amplified up to mA levels.

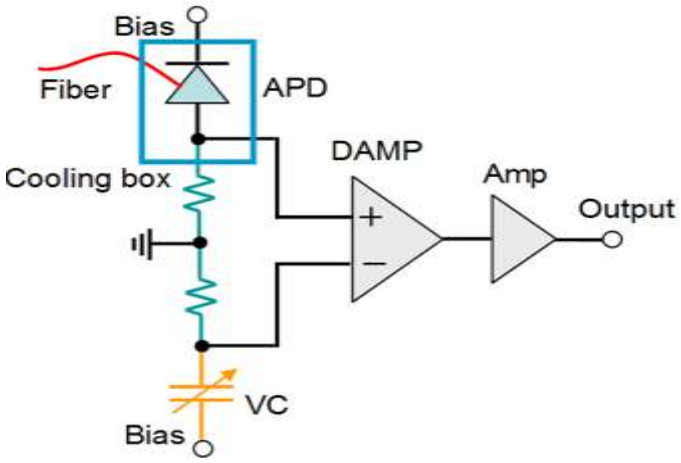

Figure 4. A basic APD detection circuit.
Source: Reproduced with thanks from Wu et al. (2011).

Figure 5. The APD's used in our designed and developed project, MATPD-06-001, from MarkTech Optoelectronics.

A discriminator circuit is mandatory, in general, to detect the pulse. A discriminator helps determine which pulses result in a count and which ones are neglected. However, in our project, we do not use a discriminator, instead we utilize this function in the software (in the DAQ routines).

Figure 3b illustrates an APD in Geiger mode and the process of avalanche photodiode operation.

Figure 4 illustrates a basic APD detection circuit with a bias voltage, upon which a practical APD light detection and spectroscopy system can be built.

Working on similar lines, our design is based upon a modern APD device; the MATPD-06-001 from MarcTech Optoelectronics, Inc. (Latham, NY, USA), a photograph of the device is illustrated in Figure 5, whereas Table 1 lists its important specifications.

Figure 6 illustrates a block diagram of our designed system, which is added to a scintillating stage to convert it into a complete gamma ray detection system. This scintillator could be a simple plastic scintillator or a sophisticated NaI/CsI scintillator. We first used a combination of plastic sheets to test our device before we could connect it to a proper scintillator.

As shown in the block schematic, an APD is used while being coupled to a transparent scintillator block. The APD is itself mounted on a cooling system (based on a commercial Thermo-Electric Cooler (TEC) plate device which cools it down to about -20°C. There is a temperature controller and Hi-voltage bias system to control the temperature as well as provide a bias voltage to the APD (we use a bias voltage of 91 V with the help of a battery farm). A current to voltage converter circuit converts the current into voltage whereas an Instrumentation-grade differential amplifier amplifies this voltage and the output is read

Table 1. Specifications of the MTAPD-06-001 APD device.

Datasheets	MTAPD-06-001 thru 004
Standard Package	1
Category	Sensors
Family	Photodiodes
Series	-
Packaging	Bulk
Wavelength	800nm
Color – Enhanced	-
Spectral Range	400nm ~1100nm
Diode Type	Avalanche
Responsivity @nm	50A/W @800nm
Response Time	300ps
Voltage – DC Reverse (Vr) (Max)	120V
Current – Dark (Typ)	50pA
Active Area	230µm Dia
Viewing Angle	-
Operating Temperature	-20^{0}C ~85^{0}C
Mounting Type	Through Hole
Package/Case	TO-46-2 Metal Can
Online Catalog	Silicon Avalanche Photodiodes
Other Names	1125-1286 MTAPD-06-001-DIG

Source: Courtesy Digi-Key Corp., Thief River Falls, MN, USA.

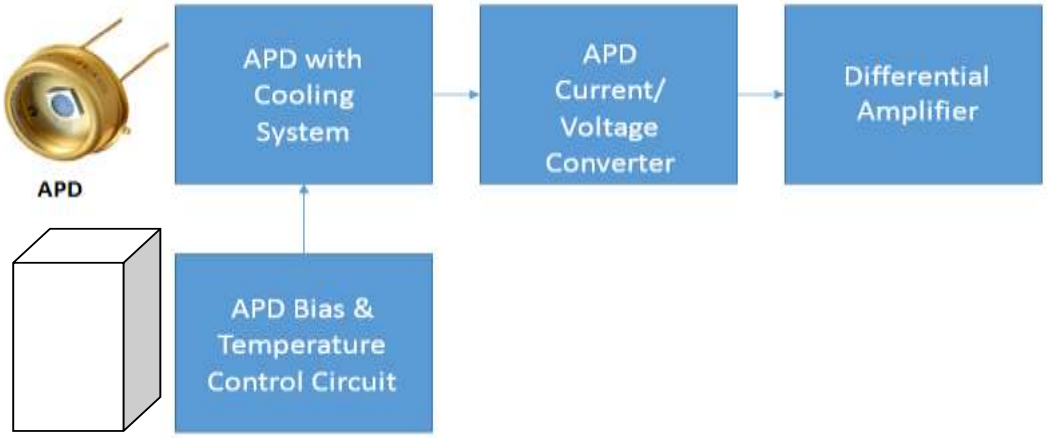

Figure 6. Our designed APD gamma detection system with a transparent plastic scintillator block.

by an oscilloscope or a Data Acquisition System. We use an Agilent/Keysight DSOX 400 MHz Digital Storage Oscilloscope for time-domain signal analysis.

Figure 7 illustrates a circuit schematic of our detector amplifier, which is based on three stages. In the first stage, an APD is biased through an appropriate quenching circuit with a bias voltage. 100 KΩ is for the Geiger Mode, for single photon detection, and 10MΩ is for the normal APD operation. The two back-to-back diodes are used for protection of the APD and amplification circuit against voltage spikes. The second stage is a current to voltage conversion system which converts the APD photo-current into voltage using a high-resistance feedback. The 2pF small-value capacitor is used for stability. The output of this stage is passed through a Low-Pass RC passive filter to the third stage which is a simple gain of 10 non-inverting voltage amplifier, which further amplifies the weak signal to a reasonable magnitude to be read by output device.

We employ a simple JFET based Operational Amplifier combination using Texas TL071C and TL072C amplifiers (TL071, 2017), however for higher precision, an instrumentation amplifier from Analog Devices, AD8421 could be used (AD8421, 2012). Working design of a detector and spectroscopy system using a specialized instrumentation amplifier device has been reported in an earlier report (Bukhari and Shah, 2016), and could be employed here replacing TL072C with necessary modifications. Techniques for constructing such circuits and laying out the

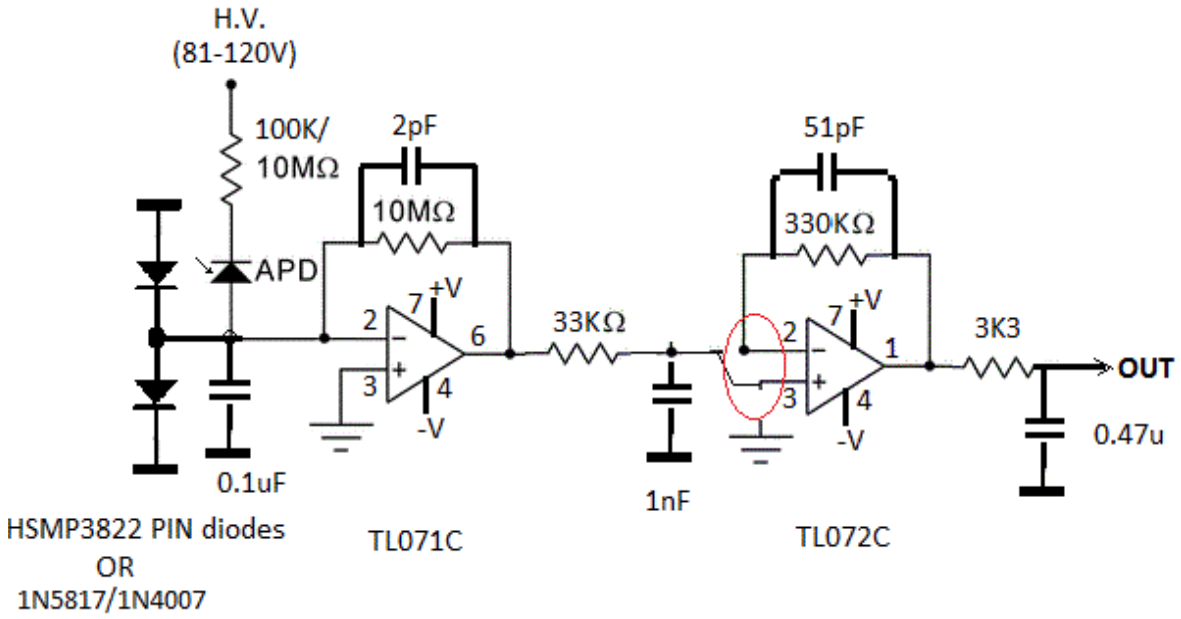

Figure 7. The schematic for our APD detector amplifier. Note that a TEC (Thermo-electric) plate is not shown in the design which is mounted underneath the APD for cooling purposes.

PCB layout for instrumentation amplifiers has been reported elsewhere (Claycomb, 2016).

Some views of the prepared prototype are given in the Figure 8a and 8b. The color code of the ribbon cable connections are; RED: +12/9V, YEL: -12/9V, GRN: 0V, ORA: Signal Output, VIOL: APD Bias Voltage (+81-120VDC), BLU: APD Bias Voltage Ground.

Figure 8c shows a view of a typical plastic scintillator, a commercial device available in market (Bicron Corp. (Canaan, CT, USA). It was quite suitable for this project, however a CsI:TaI or NaI:TaI crystal would be a much better choice, especially for spectroscopy applications.

After fabrication, the APD and Scintillator blocks are enclosed in a dark light-free enclosure, with only a small opening open for the gamma radiation to enter.

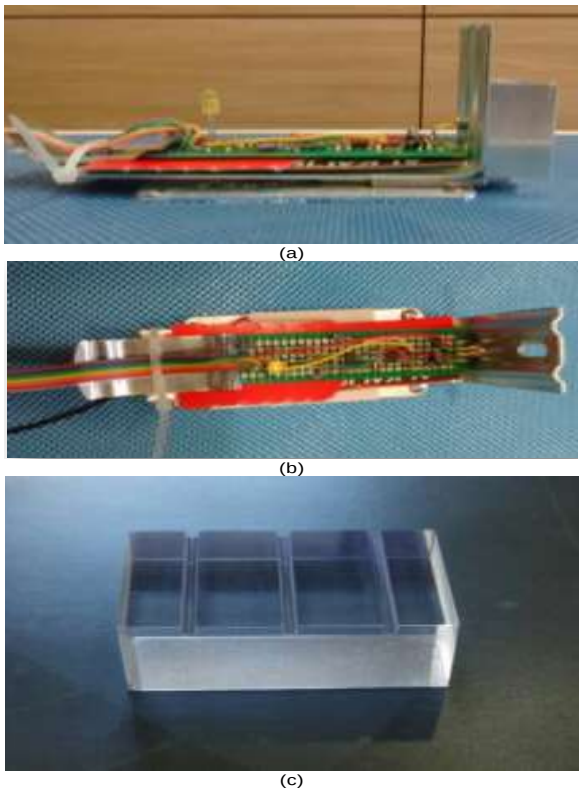

Figure 8. a) and b) Top and side views of our prepared prototype. The APD circuit board with the APD and other components are mounted on a brass frame (with an Aluminum Heat Sink with a hole in it where APD face is mounted), which has underneath it a TEC (Thermo-Electric Cooler) cold plate. c) An organic scintillator employed in the study.

RESULTS

After completion of the system, detailed tests were carried out and results were obtained. We present here our preliminary results, as shown in Figure 9, some measurements of noise as recorded with our system. The figure shows some pulses as detected with the APD system including noise, as measured with our test plastic scintillator without.

Figure 10 illustrates gamma detection events measured with an organic scintillator detector, as emanated from a Cobalt (^{57}Co) source.

Two conspicuous peaks, a primary peak at approximately 122 keV and a secondary peak at 136 keV, whereas a few low-count peaks are seen at the region of 30-60 keV.

Figure 11 illustrates a completed prototype with an

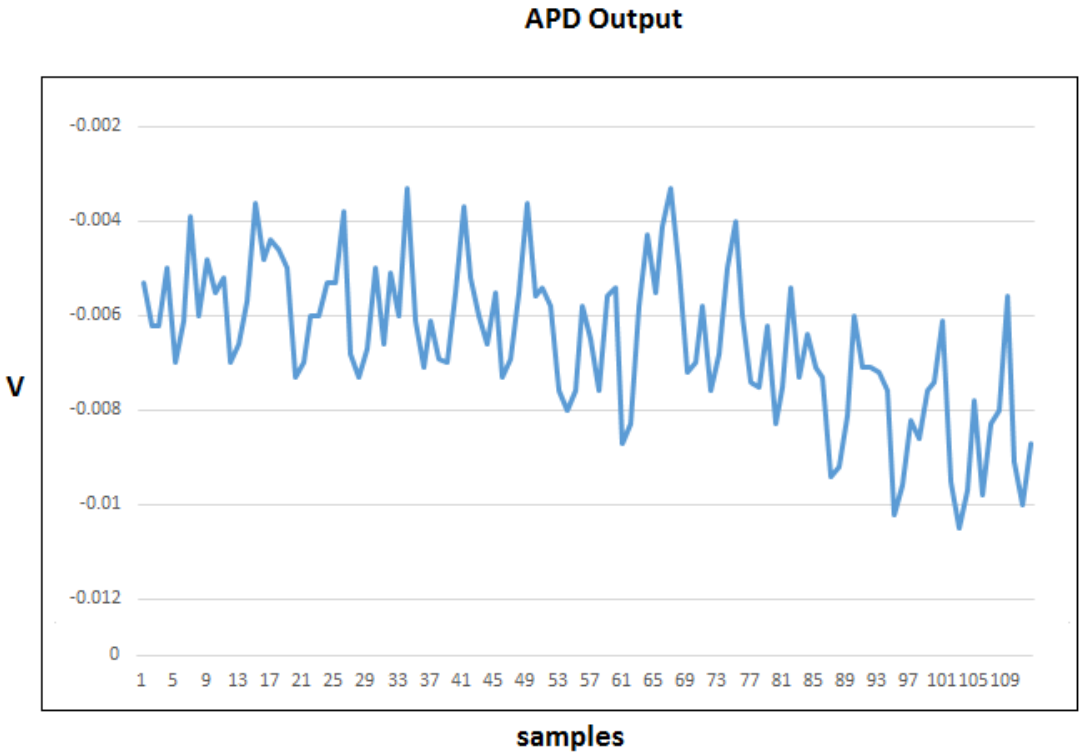

Figure 9. Noise output of our detection system showing random thermal and shot noise of extremely low magnitude along with some weak pulses.

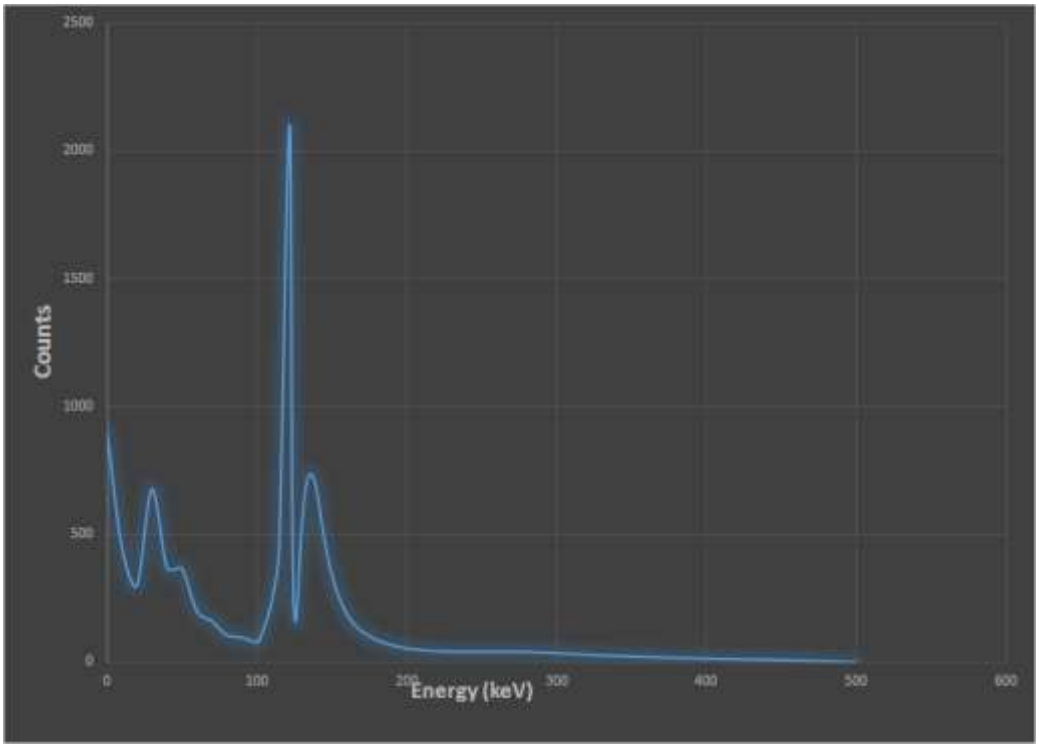

Figure 10. Gamma ray detection demonstration from a ^{57}Co source. The isotope has a primary peak at approximately 122 keV and a secondary peak at 136 keV, whereas a few low-count peaks are seen at the region of 30-60 keV (Horizontal axis Energy, in keV, vertical axis, Counts per channel).

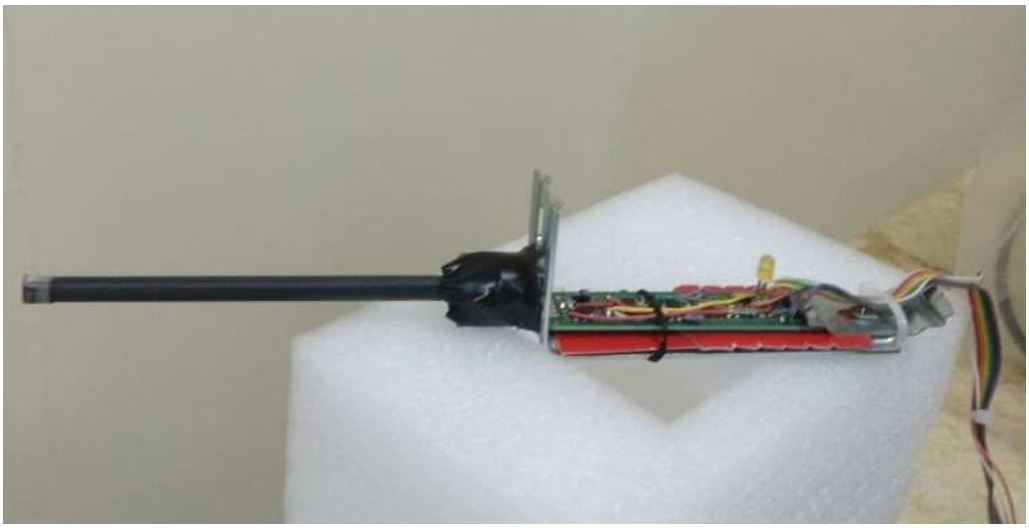

Figure 11. A completed prototype with a plastic scintillator and wave guide (both wrapped in black tape) coupled to the APD and the detection circuit.

organic scintillator (different from the one shown in Figure 8c) wrapped in black tape to block external light.

Conclusion

The design and test of a practical, simple and effective low-cost gamma detection and spectroscopy system were carried out, important details of which have been reported in this paper. The circuit designed may not be the best of its kind. With necessary modifications in the APD biasing scheme and detection circuit, both precision and efficiency of the system can be improved.

Since APD devices are finding viable usage in many other science and engineering applications, this design could be modified for use in a variety of areas. For instance, this design can be used in quantum information (Wu, 2011) and quantum computing as well.

CONFLICT OF INTERESTS

The authors have not declared any conflict of interests.

ACKNOWLEDGEMENTS

MHSB appreciates the support by the Deanship of Scientific Research, University of Jazan (under DSU grant #3125 to P.I. M. H. S. Bukhari), and the Department of Physics, University of Jazan, in setting up of *"J.U. Ultra-Low Level Quantum Measurement Laboratory"* (P.I. M. H. S. Bukhari) where this research and development activity was carried out.

REFERENCES

AD8421 (2012). Instrumentation Amplifier Data Sheet, Analog Devices (Norwood, MA). http://www.analog.com/media/en/technical-documentation/data-sheets/AD8421.pdf

Aull B (2016). Geiger-Mode Avalanche Photodiode Arrays Integrated to All-Digital CMOS Circuits. Sensors 16(4):495.

Bukhari MHS, Shah ZH (2016). Low-Noise Amplification, Detection and Spectroscopy of Ultra-Cold Systems in RF Cavities. Mod. Instrum. 5:2.

Claycomb T (2016). "How to layout a PCB for an instrumentation amplifier", TI Blogs (Texas Instruments, Dallas, TX), Oct 16th 2016.

Razeghi M (2010). Technology of Quantum Devices, Chapter 12, Single Photon Avalanche Diodes, Springer. DOI 10.1007/978-1-4419-1056-1_12

TL071 (2017). TL07xx Low-Noise JFET-Input Operational Amplifiers Datashee. Texas Instruments SLOS080N (Sept. 1978 Revised July 2017).

Tsang WT (1985). Semiconductors and Semimetals. Part D "Photodetectors". Academic Press 22.

Webb PP, Mclntyre RJ (1970). Single Photon Detection with Avalanche Photodiodes. Bull. Am. Phys. Soc. 15:813.

Wolff PA (1954). Theory of Electron Multiplication in Silicon and Germanium. Phys. Rev. 95:1415-1420.

Wu G (2011). Near-Infrared Single-Photon Detection. Photodiodes - World Activities in 2011 J-W Park (Ed.), ISBN 978-953-307-530-3, Intech Publishing (July 29, 2011).

Related Journals: